Interfacial Self-Assembly of Colloidal Nanoparticles in Dual-Droplet Inkjet Printing

*Karam Nashwan Al-Milaji, Ray Richard Secondo, Tse Nga Ng, Nathaniel Kinsey, and Hong Zhao**

The well-known coffee-ring effect causes colloidal particles to convectively transport toward the contact line of an inkjet droplet leading to a nonuniform deposition of the colloidal particles. In this work, the self-assembly of colloidal particles in a dual-droplet inkjet printing configuration to produce a nearly monolayer closely packed deposition of colloidal particles that exhibits a colorful reflection are demonstrated. By controlling the ink surface tensions and jetting parameters, the wetting droplets (the second droplet) containing colloidal polystyrene (PS) nanoparticles quickly spread over the supporting droplets (the first droplet) upon impact. The well-ordered deposition is achieved by tuning the solvent composition of the wetting droplets and functionalization of the PS nanoparticles to encourage a network formation among the colloidal particles at the air–droplet interface. The underlying self-assembly mechanism is insensitive to substrates and can be applied to many other material/substrate combinations. Finally, the origin of the color generation is highlighted, and the potential of the dual-droplet inkjet printing process is discussed for fabrication of optical devices.

1. Introduction

When a particle-laden droplet evaporates on a substrate, very often the particles form a ring at the contact line when the solvent evaporates. This well-known coffee-ring effect is a result of faster evaporation at the droplet contact line, driving the colloidal particles to convectively transport toward the droplet edges.[1–3] For applications in printed electronics, this nonuniform deposition is particularly detrimental to the device performance. The complex multibody interactions, e.g., droplet–substrate interaction, particle–substrate interaction, and droplet–environment interaction, ultimately determine the final deposition and morphology of patterns.[4–9] Various approaches have been explored to modify these interactions in order to control the contact line dynamics and/or to induce Marangoni flow driven by the surface tension gradient on the air–droplet interface, including tuning substrate wettability,[10,11] application of surfactant additives and cosolvent systems to the droplet,[12,13] vapor absorption of low-surface tension solvents to the droplet,[14] etc. In these techniques, the colloidal particles are carried back to the center of the droplet either by the depinned contact line or by Marangoni flow to suppress the coffee-ring effect. In addition, stronger interactions between colloidal particles and substrates, e.g., electrostatic and van der Waals interactions,[15] and increased adhesion through substrate treatment,[16] etc. also facilitate a uniform deposition.

Recently, attempts have been made to push the colloidal particles onto the droplet surface to facilitate the particle self-assembly at the air–droplet interface.[17] Boley et al. have employed a cosolvent system for the colloidal particles.[18] During evaporation, the colloidal particles which are well-dispersed in the solvent with a higher vapor pressure are carried to the droplet surface due to faster evaporation of this solvent component. Li et al. have accelerated the solvent evaporation rate to trap the particles at the droplet interface by elevating the environment temperature.[19] At a high environment temperature, the air–droplet interface shrinkage rate exceeds the particle diffusion rate such that the colloidal particles are captured by the descending surface, producing a particle jam which prevents them from being transported to the droplet edge. The charges of surfactant-decorated particles have also been tuned to become nearly neutral,[20,21] which promotes particle trapping at the air–droplet interface to render a homogeneous deposition.

In this work, we employ a dual-droplet configuration to transform the Langmuir–Blodgett (LB) concept to the picoliter droplets generated by inkjet printing. Deposition of monolayer nanoparticle films is achieved by a consecutive dual-droplet printing of a supporting droplet and a wetting droplet (**Figure 1**). The supporting droplet acts as the LB trough, and the wetting droplet contains colloidal nanoparticles. The colloidal particles spread over the supporting droplet surface and assemble at the interface as the solvent dries to produce a uniform, nearly

K. N. Al-Milaji, Prof. H. Zhao
Department of Mechanical and Nuclear Engineering
Virginia Commonwealth University
BioTech One, 800 East Leigh Street, Richmond, VA 23219, USA
E-mail: hzhao2@vcu.edu

R. R. Secondo, Prof. N. Kinsey
Department of Electrical and Computer Engineering
Virginia Commonwealth University
601 West Main St., Richmond, VA 23284, USA

Prof. T. N. Ng
Department of Electrical and Computer Engineering
University of California, San Diego
9500 Gilman Drive, La Jolla, CA 92093, USA

The ORCID identification number(s) for the author(s) of this article can be found under https://doi.org/10.1002/admi.201701561.

DOI: 10.1002/admi.201701561

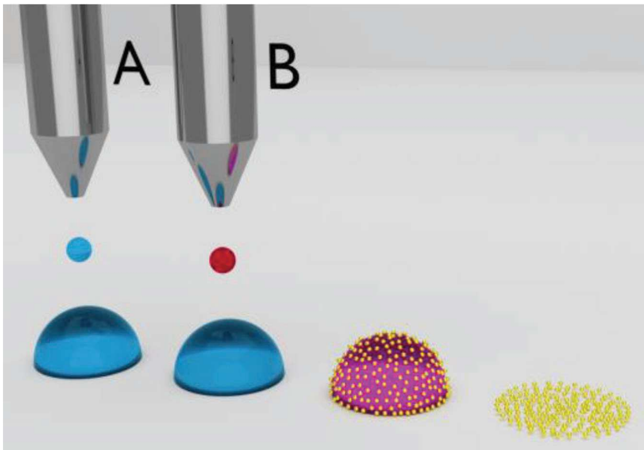

Figure 1. Schematic of the dual-droplet printing process. Blue represents the supporting droplet; red is the wetting droplet; and gold represents the PS nanoparticles.

monolayer deposition of the nanoparticles. Three main steps take place toward the monolayer self-assembly: (i) spreading of the wetting droplet and colloidal nanoparticles over the supporting droplet; (ii) nanoparticle packing and assembly at the interface between the wetting droplet and supporting droplet; and (iii) settling of nanoparticle film layer onto the substrate upon evaporation of the supporting droplet. **Figure 2** has compared the assembly mechanism during the dual-droplet printing process and those in the regular inkjet printing processes. In this study, the spreading of the wetting droplet is enabled by formulating a low-surface tension ink containing colloidal particles and a high-surface tension solvent for the supporting droplet. Deionized (DI) water was used as the solvent for supporting droplets; a mixture of ethanol/water was used as the solvent for wetting droplets. Monodispersed polystyrene (PS) nanoparticles were used as the colloidal particles.

The spreading of the wetting droplet and colloidal particles at the interface has been verified through high-speed imaging. The fate of the colloidal particles, however, differs during the solvent drying process depending on the solvent composition of the wetting droplets, functionalization, and the amount of PS nanoparticles deposited onto the supporting droplet. Some nanoparticles get trapped at the interface till the final deposition onto the substrate, while some may diffuse into the bulk of the supporting droplet. As a result, the final assembly exhibits morphologies from a nearly closely packed monolayer deposition to a fully covered but not closely packed arrangement. PS nanoparticles with different sizes have been used to fabricate optical films which exhibit different colors due to the varying optical resonance of the particles. The implication of this dual-droplet printing process in fabricating photonic crystals and devices applications is also discussed.

2. Results and Discussion

2.1. Dual-Droplet Inkjet Printing

The first step for a controlled nanoparticle assembly in the dual-droplet printing is to realize spreading of the wetting droplet onto the supporting droplet. Similar double-shot inkjet printing has been employed to print organic semiconductor films through antisolvent crystallization,[22,23] where the wetting (or spreading), dewetting, and sinking regimes were

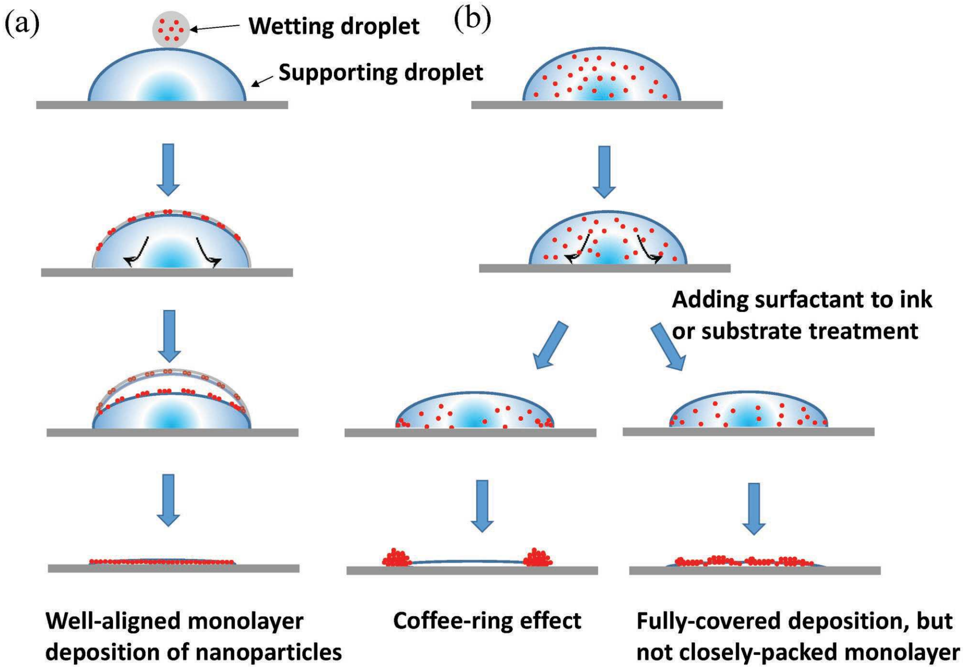

Figure 2. Schematics of a) dual-droplet printing (this work); and b) conventional inkjet printing causing either coffee-ring formation or not well-controlled deposition morphology.

identified when a microdroplet was added onto a chemically different sessile droplet. Surface tension of the wetting droplet needs to be lower than that of the supporting droplet to enable initial spreading, as shown in the spreading parameter $S = \gamma_{SG} - (\gamma_{SW} + \gamma_{WG}) > 0$, where γ is the interfacial surface tension; subscripts S, W, and G represent supporting droplet, wetting droplet, and gas phase, respectively. The interfacial surface tension between miscible solvents is negligible in this system. We use DI water (surface tension of 72.5 mN m^{-1}) to generate the supporting droplets and ethanol (surface tension of 21.8 mN m^{-1}) or a mixture of ethanol/water for the wetting droplets. The highest surface tension used for the wetting droplets is 28.51 mN m^{-1} for 50 wt%/50 wt% ethanol/water mixture at 20 °C.[24] The modified *Weber* number,[23] $We' = \rho_W v_W^2 d_W^3 / \gamma_S \left(\frac{V_S}{f(\theta)}\right)^{2/3}$, compares the inertial energy of the wetting droplet to the deformation energy of the supporting droplet surface, where ρ_W is the density of the wetting droplets, v_W is the impact velocity of the wetting droplet, d_W is the wetting droplet diameter, V_S is the supporting droplet volume, $f(\theta) = \pi \frac{2 - 3\cos\theta + \cos\theta^3}{3(1-\cos\theta)^3}$, and θ is the contact angle of the supporting droplet on the substrate. A smaller We' favors spreading of the wetting droplets, and a larger We' tends to bring the wetting droplet into the supporting droplet and enhances chaotic mixing of the wetting and supporting droplets. Therefore, smaller wetting droplets with slower impact speeds and larger supporting droplets with higher contact angles will facilitate spreading of the wetting droplet. The derivation of We' and the effect of impact speed of the wetting droplet are provided in the Supporting Information.

In this work, the supporting droplet is generated by multiple bursts of inkjet droplets, equivalent of a ≈110 nL water droplet. One wetting droplet with a volume of ≈550 pL is deposited onto the supporting droplet by a secondary printhead. The jetting configurations described in the Experimental Section were used in all the experiments unless noted otherwise. The dimensionless We' was kept <0.42 during all the experiments. High-speed photography was employed to capture the wetting droplet impact onto the supporting droplet, revealing the real-time impact kinetics.

Upon the initial impact, as shown in **Figure 3**a, the wetting droplet creates a crater on the supporting droplet surface. In less than 20 ms, however, the latter surface is totally recovered after a few oscillation and damping cycles. Only one oscillation is shown in Figure 3a. Immediately after the droplet impact, the PS nanoparticles on the supporting droplet surface move along with the Marangoni flow created by the ethanol/water surface tension gradient. A film of the colloidal PS nanoparticles can also be identified in Figure 3b. Individual PS nanoparticles collide and assemble into larger islands and monolayer networks at the interface by lateral capillary force (i.e., particle–interface interactions),[25,26] which are trapped at the air–water interface in an energetically favorable state due to the interfacial deformation caused by the fractal shape of the agglomerates[27] compared to individual spherical nanoparticles. In addition, the quick evaporation of ethanol solvent in the wetting droplet also contributes to the network formation on the supporting droplet surface. During evaporation of the supporting droplet, the PS particle film is maintained at the air–water interface, further being compressed by the reduced surface area. When the water solvent in the supporting droplet completely evaporates, a deposition of PS nanoparticles forms as shown in the last image in Figure 3b. The videos of the wetting droplet impact and PS nanoparticle assembly during solvent evaporation are included in the Supporting Information.

The example in Figure 3b shows a nearly monolayer closely packed assembly of PS nanoparticles (more characterization in the following sections), which is enabled by a successful wetting droplet spreading and a trapped nanoparticle film on the supporting droplet surface. However, some PS nanoparticles, which are originally located at the air–water interface, may diffuse into the bulk of the supporting droplet, depending on the solvent composition of the wetting droplets, the functional groups on the PS particles, and the amount of nanoparticles deposited on the supporting droplet. The morphology of PS nanoparticle assembly and their forming mechanisms under various conditions are discussed in the following sections.

2.2. Effect of Solvent Composition on the PS Nanoparticle Deposition

In order to study the effect of solvent composition in the wetting droplet on the PS nanoparticle deposition, we have selected the aldehyde/sulfate-functionalized PS particles. The detailed

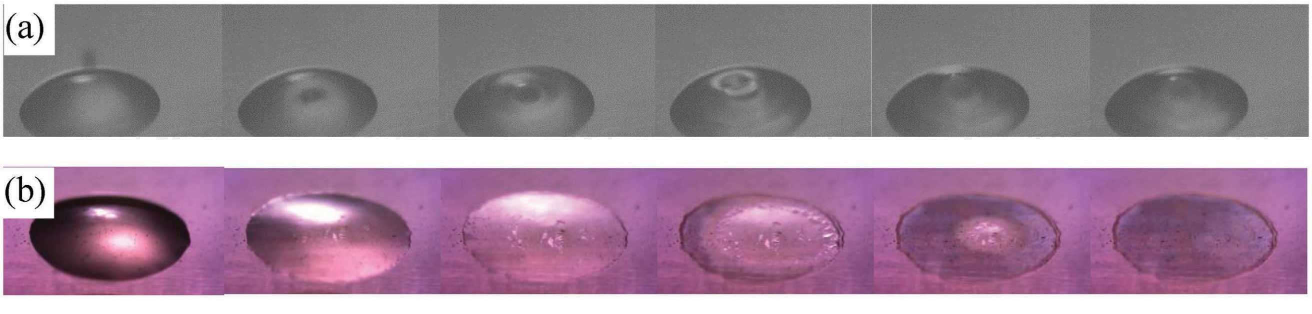

Figure 3. a) Wetting droplet impact onto a supporting droplet by high-speed imaging (time interval of 0.2 ms between each image). b) Images of PS nanoparticle film floating on the surface during the evaporation process (t = 0, 51.5, 69.9, 78.3, 80.3, and 80.6 s). The suspension of sulfate-functionalized PS nanoparticles prepared with 100% ethanol is used for the wetting droplets, three of which are deposited onto the supporting droplet. The PS nanoparticle size is 100 nm in diameter.

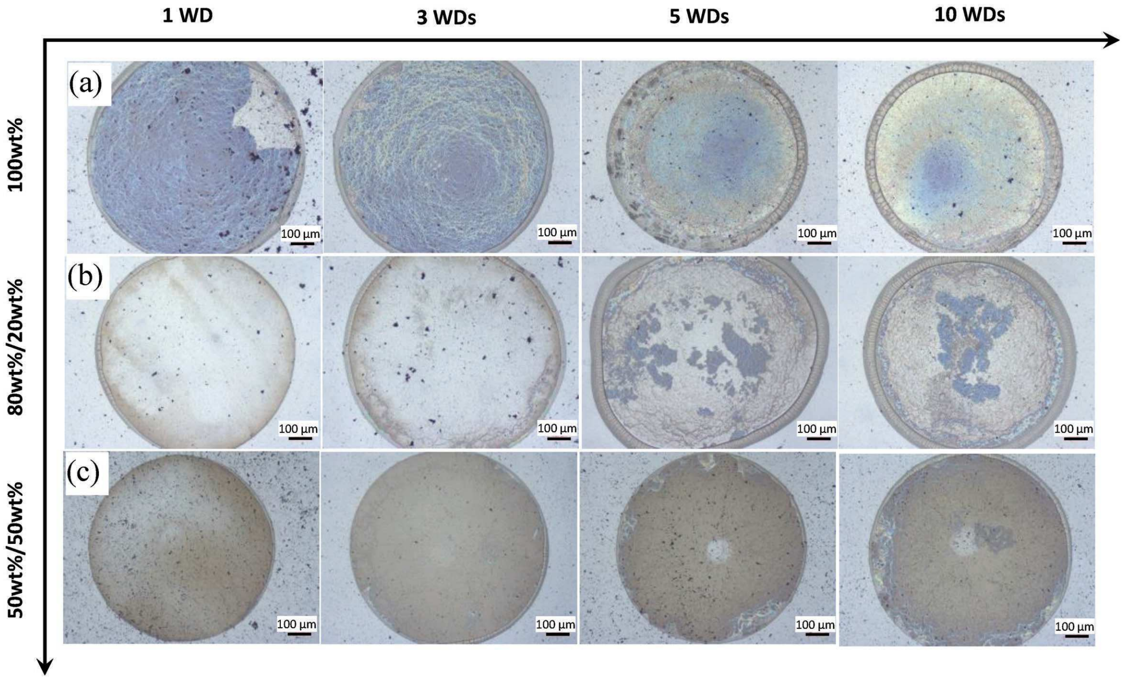

Figure 4. Optical images of aldehyde/sulfate-functionalized PS nanoparticle deposition at a) 100% ethanol; b) 80 wt%/20 wt% ethanol/water; and c) 50 wt%/50 wt% ethanol/water-diluted inks in the wetting droplets. The four columns represent various nanoparticle amounts of one, three, five, and ten wetting droplets (WDs), respectively. The scale bar is 100 µm. A dopamine-treated substrate is used. The PS nanoparticle size is 100 nm in diameter.

information about the functionalized particles is provided in Table S1 in the Supporting Information. The as-received aqueous suspension of aldehyde/sulfate-functionalized PS particles was diluted in 100% ethanol, 80 wt%/20 wt% ethanol/water, and 50 wt%/50 wt% ethanol/water to formulate the inks for wetting droplets with a PS nanoparticle concentration of 10 mg mL^{-1}. The amount of nanoparticles is controlled by the number of wetting droplets deposited onto the supporting droplet.

The ink diluted with 100% ethanol gives the best nearly monolayer PS nanoparticle deposition especially for a lower nanoparticle amount (e.g., one wetting droplet), indicated by the blue structural color as shown in **Figure 4**a. This can be attributed to the scattering of resonant modes within the spherical nanoparticle cavities (see Section 2.6). The nearly monolayer PS nanoparticle deposition is confirmed by scanning electron microscopy (SEM) images (Figure S3, Supporting Information). The incomplete coverage of the entire droplet footprint is due to the insufficient particle density in the single wetting droplet, as well as some nanoparticle deposition on the contact line edges. The gray "ring" at the periphery of the deposition is a result of reflective light scattering in the light microscopic image, indicating a different assembly mechanism. It is hypothesized that the surface modifier dopamine[16] attracts and captures the PS particles at the edges through Derjaguin–Landau–Verwey–Overbeek (DLVO) interactions.[15] This likely occurs when the wetting droplet spreads on the supporting droplet upon impact. It is worth noting that we purposely do not use the term "coffee ring" because it has totally different forming mechanisms. The traditional "coffee ring" forms due to the evaporation-induced convective capillary flow carrying the colloidal particles toward the contact line, while the ring formed in this dual-drop printing process is attributed by the attractive interactions between the interface-trapped particles and the dopamine-coated substrate. Positively charged groups from protonation of amine groups of the dopamine surface[28] could attract the negatively charged PS particles at the droplet contact line. The ring formation consumes some of the PS particles; however, it does not change the self-assembly mechanism in the majority of the deposition for a nearly closely packed monolayer.

For high PS nanoparticle amounts (e.g., 5–10 wetting droplets), the monolayer films are compressed during solvent evaporation, leading to formation of multilayers and/or buckled films. As a result, the structural color fades away (Figure 4a), because the order of arrangement decreases in the PS particle film which broadens and weakens the resonance. The profiles of blue color contrast (BCC) along the deposition radius are plotted in **Figure 5** for each of the optical microscope images. The BCC exhibits significant correspondence in monolayer deposition across the droplet footprint. The image analysis and postprocessing are described in details in the Materials and Methods. For the optimum nanoparticle amount, the BCC is nearly constant over the entire droplet corresponding to the one wetting droplet in Figure 5a, while for a higher nanoparticle amount, the BCC is high in the center and gradually decreases toward the edge of the deposition. In those cases, the excess nanoparticles at the air–droplet interface are pushed toward the edge of the supporting droplet and are captured by the dopamine-coated substrate at the contact line, which is shown by the widen rings at the periphery of the droplet deposition. For the same reason, less ordered multilayer

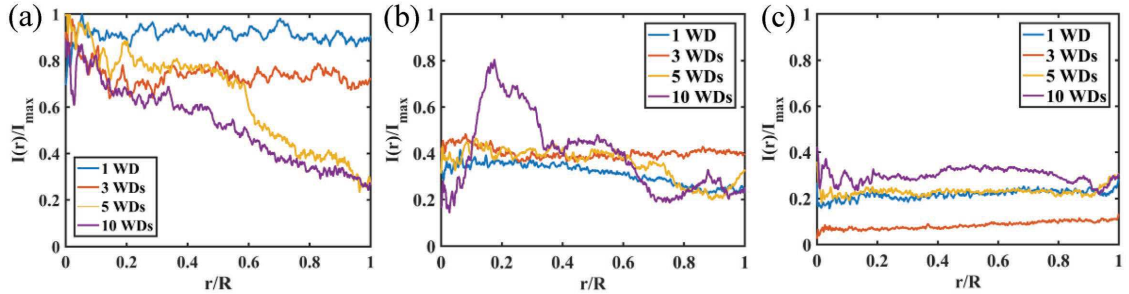

Figure 5. Normalized BCC from center to periphery on the nanoparticle depositions in Figure 4 using a) 100% ethanol-diluted inks, b) 80 wt%/20 wt% ethanol/water-diluted inks, and c) 50 wt%/50 wt% ethanol/water-diluted inks for the wetting droplets. WD: wetting droplet.

deposition forms toward the contact line region which reduces the BCC. Figure S3a (Supporting Information) shows the SEM images of the PS nanoparticle deposition under various particle amounts deposited onto the supporting droplet. The nearly monolayer depositions at lower particle amounts are compared with the multilayer agglomerates at higher particle amounts.

As water is added into the wetting droplet solvent, e.g., 80 wt%/20 wt% ethanol/water, the structural color of the final deposition disappears (Figure 4b), indicating the absence of closely packed monolayer PS deposition. Fragments of blue color films present on the depositions at high particle amounts. We hypothesize that during the supporting droplet evaporation, some hydrophilic aldehyde/sulfate-functionalized PS particles diffuse and mix into the supporting droplet due to the addition of water solvent. In addition, electrostatic repulsion between the particles also facilitates the nanoparticles to diffuse into the supporting droplet. Different from the assembly driven by the dominant particle–interface interactions (Figure 2a), the particles experience an intricate combination of particle–interface, particle–substrate, and particle–flow field interactions (Figure S4, Supporting Information). The evaporation-driven capillary flow inside the supporting droplet carries those particles toward the edges. When they touch the dopamine-coated substrate, the PS particles likely are captured and immobilized on the substrate. The final deposition morphology is attributed to the particles residing at the interface (self-assembled blue color PS fragments) and the particles in the bulk of the supporting droplet.

When more water is added into the wetting droplet solvent, e.g., 50 wt%/50 wt% ethanol/water, as shown in Figure 4c, none of the depositions demonstrates any blue color. Please refer to Figure S3b (Supporting Information) for the SEM images of the deposition. It is worth pointing out that adding water to the wetting droplet solvent does not change the spreading of the wetting droplet.[23] The surface tension of the 50 wt%/50 wt% ethanol/water is still much lower than that of water. The wetting droplet spreads on the supporting droplet upon impact as verified by the high-speed imaging. However, majority of the PS nanoparticles diffuse into the supporting droplet during the evaporation. At the same time, the gray "ring" at the periphery of the deposition does not grow much as the nanoparticle amount increases, which also supports that only a small fraction of the PS nanoparticles remained at the interface. Figure 5b,c clearly correlates the orderliness of the assembly to the BCC intensity.

2.3. Effect of Functional Groups on the PS Nanoparticle Deposition

Three different kinds of functionalized PS nanoparticles, i.e., carboxyl-, sulfate-, and aldehyde/sulfate-functionalized PS nanoparticles, diluted in 100% ethanol are used to generate the wetting droplets. The detailed information about the functionalized nanoparticles is provided in Table S1 in the Supporting Information. The nanoparticle concentration in the wetting droplets is kept the same as 10 mg mL^{-1}. Sulfate functional groups are the most hydrophilic in nature due to its acidity. However, the sulfate-PS particles have a surface charge density about ≈1/12th of that on the aldehyde/sulfate- and carboxyl-PS particles. The fewer functional groups and weaker electrostatic interactions between particles facilitate formation of a particle "skin" on the air–droplet interface which consists of a monolayer of nanoparticles and multilayers of agglomerates. The SEM images of the nanoparticle deposition for one and five wetting droplets are shown in Figure S5 in the Supporting Information. Compared to the aldehyde/sulfate-PS particles, a relative uniform blue color across the deposition, yet not as bright, is obtained for the sulfate-PS particles for various amounts of nanoparticles deposited onto the supporting droplet (**Figure 6**a).

Sulfate-PS nanoparticles demonstrate more robustness in achieving the closely packed deposition, against addition of water into the wetting droplet solvent. When water is added to the wetting droplet solvent, e.g., 80 wt%/20 wt% ethanol/water, a monolayer of sulfate-PS particles as well as their agglomerates are trapped at the interface, indicated by the bluish-brown islands on the final deposition, as shown in Figure 6b for the one and three wetting droplets. An incomplete coverage of the deposition with the three wetting droplets supports the hypothesis of agglomeration formation, as compared to the full coverage and higher BCC intensity with 100% ethanol. The deposition still shows a certain degree of orderly structure for higher nanoparticle amounts. Aldehyde/sulfate- and carboxyl-PS particles, on the other hand, exhibit stronger hydrophilicity and repel each other due to their higher surface charge densities. Some particles diffuse into the bulk of the supporting droplet as a result of stronger hydrophilicity

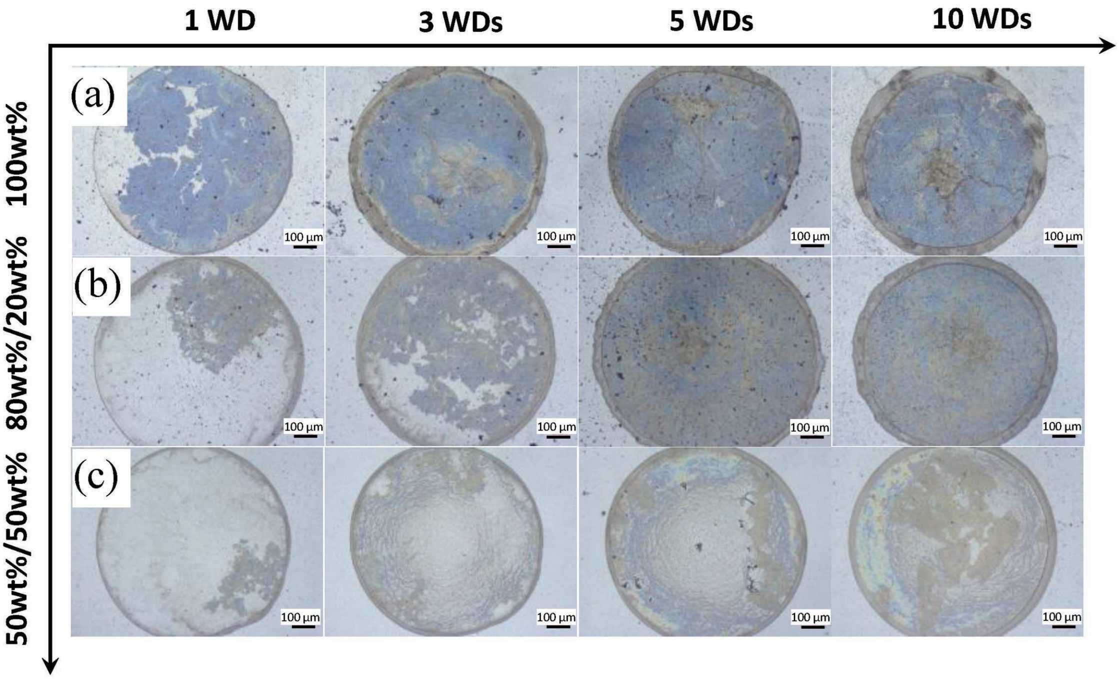

Figure 6. Optical images of sulfate-functionalized PS nanoparticle deposition at a) 100% ethanol; b) 80 wt%/20 wt% ethanol/water; and c) 50 wt%/50 wt% ethanol/water-diluted inks in the wetting droplets. The four columns represent various nanoparticle amounts of one, three, five, and ten wetting droplets, respectively. The scale bar is 100 µm. A dopamine-treated substrate is used. The PS nanoparticle size is 100 nm in diameter.

and electrostatic interactions. The final deposition shows a nonuniform irregular morphology contributed by particles residing at the air–droplet interface and in the bulk of the supporting droplet.

Compared to the aldehyde/sulfate- and the sulfate-PS particles, carboxyl-PS particles have not produced decent orderly structures even with 100% ethanol. The deposition morphologies are shown in Figure S6 in the Supporting Information. Carboxyl groups are strongly hydrophilic, which can lose a proton to form a negatively charged carboxylate ion (COO−). Although carboxyl groups are less hydrophilic than sulfate groups in nature, the number of carboxyl groups per particle is more than 10 times larger than that of sulfate groups on a sulfate-PS particle (Table S1, Supporting Information), providing more affinity toward water. For the aldehyde/sulfate-PS particles, a large number of aldehyde function groups alternate with fewer sulfate groups on the PS particle surface, which reduces the hydrophilicity of these PS nanoparticles. Therefore, with comparable charge densities of carboxyl and sulfate groups on the PS nanoparticle surfaces, the carboxyl-PS particles experience stronger affinity to water than the aldehyde/sulfate-PS particles. As a result, the carboxyl-PS particles readily diffuse into the supporting droplet during solvent evaporation, and the final deposition exhibits absence of orderly arrangement.

2.4. Effect of Substrate on the PS Nanoparticle Deposition

In this dual-droplet printing process, the colloidal particles are spread and trapped at the air–droplet interface, eliminating the particle–fluid and particle–substrate interactions. Theoretically, the closely packed nanoparticle deposition should be transferrable to other substrates. In this study, an isopropyl alcohol-cleaned polyethylene terephthalate (PET) substrate is compared to the dopamine-coated glass slide to investigate the effect of substrate on the deposition morphology. The static water contact angles on the PET substrate are about 70°. The printing parameters, e.g., 100% ethanol dilution as the wetting droplet solvent, sulfate-PS nanoparticles, and wetting droplets of one, three, five, and ten, are applied. As expected, a blue-colored nanoparticle deposition on the PET substrate indicates a well-ordered nanoparticle assembly as shown in **Figure 7**a. For the deposition with only one wetting droplet, a broken gray ring forms along circumference of the deposition, probably due to the local contact line receding. For higher nanoparticle amounts, the excess nanoparticles assist the contact line pinning resulting in continuous gray rings. Different from dopamine-coated substrates, the rings on the periphery of the deposition on PET substrates are less severe than their counterparts, indicating weaker interaction between the interface-trapped nanoparticles and the PET substrate. Since fewer nanoparticles are consumed at the contact line and the supporting droplet possesses a smaller footprint (due to larger contact angles), more wrinkling and folding occur on the deposition with five and ten wetting droplets.

When a wetting droplet with 50 wt%/50 wt% ethanol/water is deposited onto the supporting droplet, obvious coffee ring formation has been demonstrated on the PET substrate. For lower nanoparticle amounts (e.g., one and three wetting droplets), as shown in Figure 7b, the contact line depins during the supporting droplet evaporation, pushing the particles to a pinned spot (e.g., a local defective site) on the contact line.

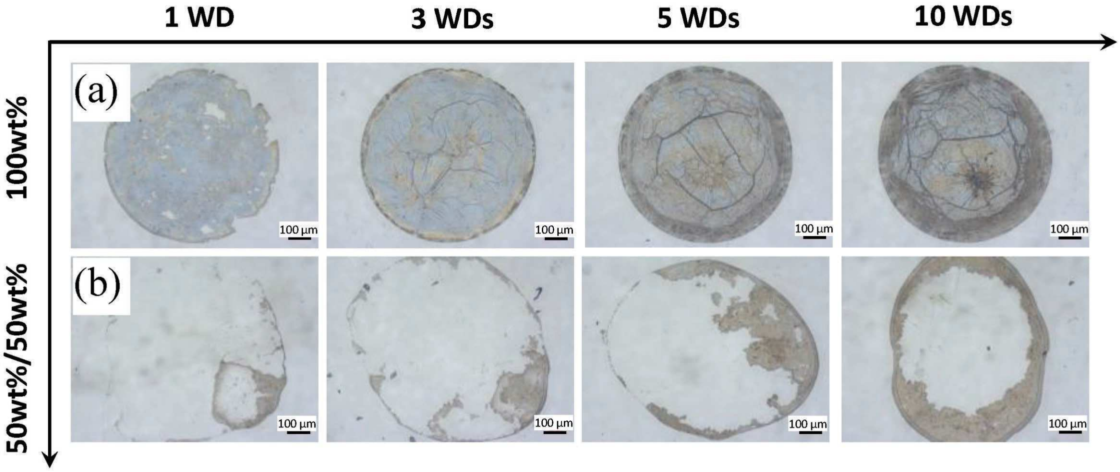

Figure 7. Optical images of sulfate-functionalized PS nanoparticle deposition on a PET substrate at a) 100% ethanol and b) 50 wt%/50 wt% ethanol/water-diluted inks in the wetting droplets. The four columns represent the four conditions of one, three, five, and ten wetting droplets, respectively. The scale bar is 100 µm. The PS nanoparticle size is 100 nm in diameter.

For higher nanoparticle amounts (e.g., five and ten wetting droplets), the contact line is pinned, assisted by the particle deposition from the interface. The majority of the nanoparticles are diffused into the supporting droplet and carried to the contact line by the evaporation-induced capillary flow. On the other hand, the not-so-obvious coffee ring formation on the dopamine-coated substrate is probably due to DLVO interactions and possible surface roughness effect. Particles inside the supporting droplet are attracted and deposited onto the dopamine-coated substrate during their transport to the edges.

Therefore, when the particles are successfully trapped and maintained at the air–droplet interface, the particle–interface interaction dominates and a monolayer deposition of the colloidal particles will be obtained. The self-assembly process is insensitive to substrates. When some particles diffuse and migrate into the bulk of the supporting droplet, however, the final particle deposition does not possess the close packing any more due to the introduced particle–flow field and particle–substrate interactions. They may produce a coffee ring if the substrate is relatively smooth (e.g., PET) and the particles deposit in the proximity of the contact line; or they may still produce a "uniform" deposition, but not closely packed one, if the substrate is coated with absorbing polymers or treated with oppositely charged surfactants to capture those particles.

2.5. Discussion

In all the previous studies, including the ones manipulating capillary flows inside colloidal droplets and those pushing the particles to the air–droplet interface, the particle depositions are more uniform comparing to coffee-ring deposition, but they usually do not exhibit closely packed orderly assembly. Different from these previous studies, this dual-droplet printing directly deposits and spreads the particles on the interface following the quick spreading and evaporation of wetting droplets. Under the right conditions of functional groups on the particles, and solvent composition of the wetting droplet, these colloidal particles can self-assemble into a particle film layer on the surfaces of the supporting droplets. Finally, a nearly monolayer and closely packed particle assembly is obtained on the substrate. Compared to other self-assembly of nanoparticle and nanowires at the air–water interface,[29,30] our approach combines the nanoparticle self-assembly and drop-on-demand into one printing process.

During the dual-droplet printing, the wetting droplet spreading is controlled by surface tensions and volume ratio of the wetting droplet and supporting droplet, as well as the impact speed of the wetting droplet. The spreading of the wetting droplet carries the particles to spread on the supporting droplet surface forming small or big islands of nearly closely packed particles depending on the particle amount deposited onto the supporting droplet. The key to a perfect monolayer deposition is to keep these particles on the supporting droplet surface during evaporation. The solvent composition in the wetting droplet and functionalization of the colloidal particles determine if those particles are kept on the surface or diffused into the bulk of the supporting droplet. This nanoparticle self-assembly mechanism is superior to the mechanisms of pushing the nanoparticles from the bulk to the droplet surface, since in the latter configurations, there are always a small amount of particle depositions following the capillary flow toward the droplet edges. In addition, when the particles are gradually transported onto the droplet surface, overlapping and particle agglomeration could occur. As a result, absence of orderly arrangement of the nanoparticles (yet relatively uniform deposition) is usually obtained in the final deposition morphology. On the other hand, the self-assembly mechanism during the dual-droplet printing process enables not only a uniform, but also nearly monolayer closely packed, assembly structure, which can bring potential applications in printed electrical and optical functional devices.

2.6. Implication in Printed Optical Devices

The capability to fabricate and control the assembly and periodic arrangement of colloidal particles is significant, especially

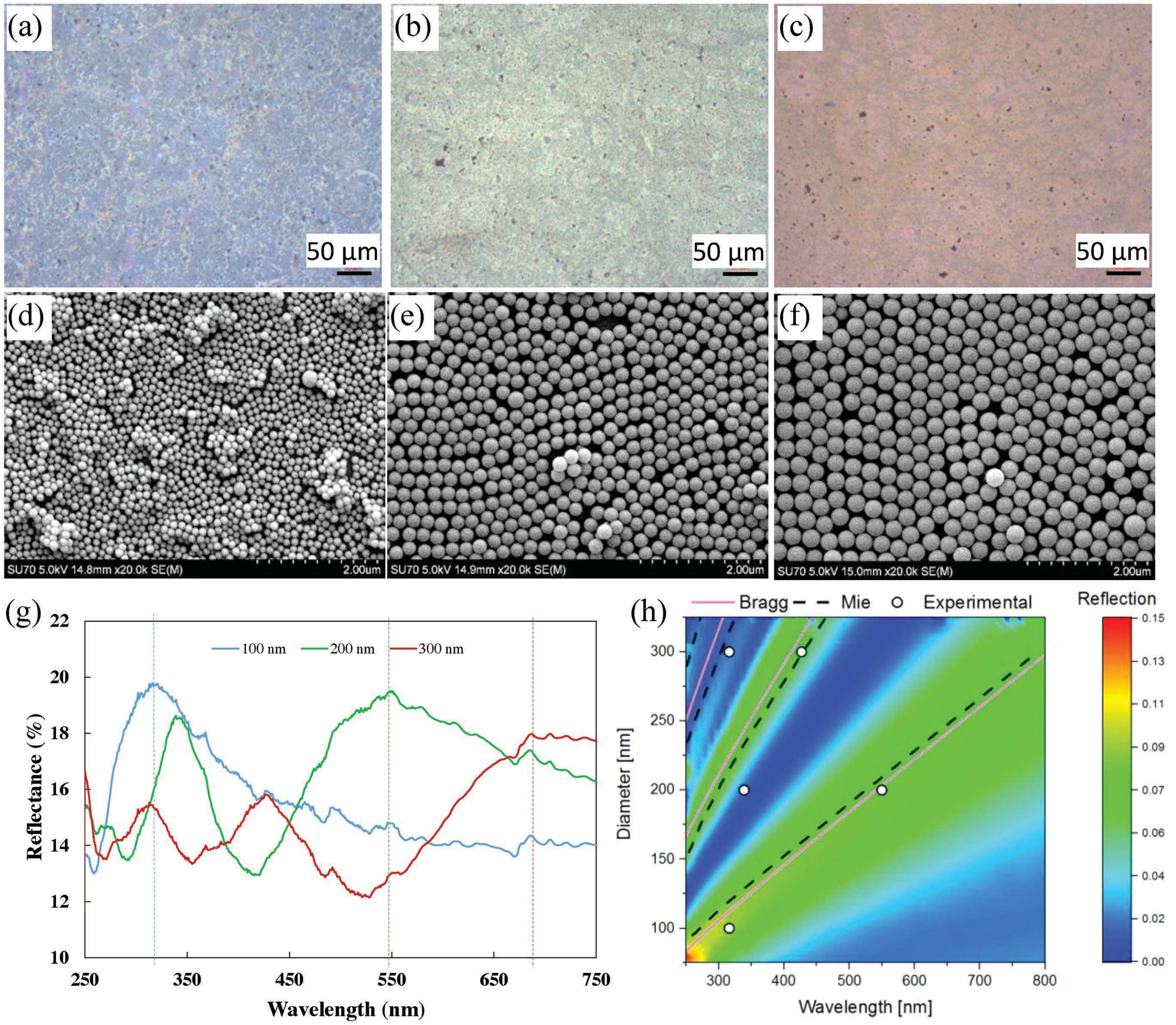

Figure 8. Optical images of PS nanoparticle assembly with diameters of a) 100 nm, b) 200 nm, and c) 300 nm. The scale bar is 50 µm. d–f) SEM images of these assembly of (a–c). The scale bar is 2 µm. g) UV–vis reflection spectra; h) comparison of the full-field simulation, the Braggs calculations (pink solid line), the Mie calculations (black dotted line), and the measured reflection peak locations (circles).

when they work as photonic crystals[31] in fast-response sensors,[32,33] displays and color filters,[34–36] and anticounterfeiting features.[37] Various approaches, e.g., photolithography templating,[38] combination of additive pattering and self-assembly,[8] and inverse opal photonic crystals,[39] have been employed for patterning colloidal particles. Among those, inkjet printing provides an efficient way to pattern the colloidal particles into functional devices.[40]

In this study, we have fabricated optical films with the self-assembled PS nanoparticles by the dual-droplet printing process. As shown in **Figure 8**a–c, these self-assembled PS particles display structural colors that strongly depend on the assembly morphology and diameter of the PS particles. Figure 8d–f shows the SEM images of those assembly structures. Larger nanoparticle sizes result in more ordered assembly, while smaller ones have exhibited some overlapping or multilayers of deposition locally. Figure 8g presents the measured reflection spectra with different PS nanoparticles of 100, 200, and 300 nm, which exhibit one single peak, double peaks, and triple peaks, respectively. The first-order peaks red-shift from 316 to 548 and ≈690 nm as the particle size increases from 100 to 300 nm, and the reflection peaks become broader in wavelength. The average offset in the reflection spectra (12%–13%) is likely attributed to the dopamine layer, whose spectrum is provided in the Supporting Information.

To understand the origin of the film's reflection spectra, full-field simulations of the PS nanoparticle assembly with particle diameters ranging from 75 to 325 nm were conducted using the finite element method (COMSOL Multiphysics). The reflection normal to the surface is calculated for a tightly packed hexagonal monolayer of PS nanoparticles on a silicon dioxide substrate, where the wavelength-dependent refractive index of PS was assumed to be of bulk PS in the material database of an ellipsometer from J. A. Woollam. The results are shown in Figure 8h, and the reflection peaks observed in experiment are marked as circles. In general, we achieved a good agreement in the peak locations between the simulation and the experiment, while the discrepancies at short wavelengths (e.g., <300 nm) can be attributed to variations in the refractive index of the PS nanoparticles as compared to the bulk PS. The good agreement between the simulated and the experimental reflection spectra indicates the good quality of the printed PS nanoparticle assembly for engineering applications in optics.

Due to the size of the particles being on the order of the wavelength of light, the optical response is most likely attributed to Mie resonances. In this case, we also plot the resonance peak spectral position as determined from analytical Mie theory[41] (black dotted lines in Figure 8h) for spherical particles on a substrate and obtain excellent agreement between the simulation and experimental results. However, Mie theory can be difficult to calculate for many cases, and a simpler approach that provides guidance would be useful. In this case, the periodic assembly of the monolayer is treated as a diffractive surface, which occurs due to the far-field interference of the many sources of scattered light (e.g., nanoparticles). As a result, we can approximate the position of the reflection peaks using Bragg's formalism $\lambda_{\mathrm{R,peak}} = n_{\mathrm{eff}}\, d(\sin\theta_i + \sin\theta_m)/m$,[42] where $\lambda_{\mathrm{R,peak}}$ is the peak reflection wavelength, m is the order of diffraction, n_{eff} is the refractive index adjusted by the packing fraction and the surrounding medium, d is the particle diameter, and θ_i and θ_m are the angles of incidence and observation from the normal direction, respectively. The reflection peak determined from Bragg formalism is shown in comparison to the prior methods in Figure 8h. Although this approach leads to some additional error in the predicted resonance position, the ease of the formula makes it a useful method to obtain an estimate for the optical response for a particular film without the need for expensive numerical software or complex analytical calculations.

3. Conclusion

In summary, we have demonstrated the ability to produce nearly monolayer closely packed depositions of PS nanoparticles through a novel dual-droplet inkjet printing process. Acting as a LB trough, a supporting droplet is deposited on the substrate followed by a wetting droplet which contains colloidal particles. The nanoparticles spread at the supporting droplet surface as a result of the wetting droplet spreading. A particle network forms among the colloidal particles when the nanoparticles are trapped and maintained at the interface during the solvent evaporation. Well-ordered monolayer deposition is obtained where the colloidal nanoparticle–interface interaction is the main driving force. When some particles diffuse and mix into the supporting droplet, due to addition of water into the wetting droplet, higher nanoparticle amounts, more surface charge density on the nanoparticles, etc., the well-ordered structure disappears in the particle assembly. The final deposition morphology is a result of particles trapped at the air–droplet interface and particles diffused into the bulk of supporting droplet, therefore following the capillary flow inside the supporting droplet.

The nearly monolayer closely packed structure brings unique structural colors on the printed features. We fabricated optical films exhibiting different colors depending on the nanoparticle sizes. This study suggests a new printing strategy to control the colloidal particle deposition with well-ordered monolayer structures. This printing process is not limited to PS nanoparticles and also insensitive to substrates. It holds enormous potentials to assemble functional colloidal particulates for applications in printed optical and electrical devices.

4. Experimental Section

Materials: Microscope glass slides (25 mm × 75 mm) were obtained from VWR. PET films (MELINEX ST505) with 125 µm thickness were supplied by TEKRA, a Division of EIS, Inc. Aldehyde/Sulfate latex beads (4% w/v, 0.1 µm), Sulfate latex beads (8% w/v, 0.1, 0.2, and 0.3 µm), and Carboxyl latex beads (4% w/v, 0.1 µm) were purchased from Thermo Fisher Scientific. Tris(hydroxymethyl)aminomethane (tris) (99.8% purity), 2-(3,4-Dihydroxyphenyl)ethylamine hydrochloride (dopamine), and hydrochloric acid (37% purity) were purchased from Sigma-Aldrich. DI water with a resistivity of 18.2 MΩ × cm was produced by Direct-Q water purification system (Millipore Sigma). KOPTEC ethanol (99.5% purity) was acquired from VWR. All chemicals were used as received without further purification.

Substrate Treatment: All glass substrates were first cleaned with solvents following the order of hot soapy water, acetone, and isopropanol, then rinsed with DI water, and dried by a clean-compressed air. The cleaned substrates were further treated with plasma for 5 min (PDC-001-HP, 115 V from Harrick Plasma) to ensure that the substrates are thoroughly clean. To control the substrate wettability and enhance contact line pinning, the cleaned substrates were chemically treated with dopamine accordingly. The cleaned glass slides were immersed vertically in a freshly prepared dopamine aqueous solution (5 mg mL^{-1}) with pH buffer of 8.5 (1.2 mg mL^{-1} tris) to initiate the oxidative self-polymerization reaction. After 24 h of reaction, the substrates were rinsed with ethanol and DI water to remove the physically absorbed and unreacted dopamine particles, and dried at 40 °C for 10 min using a vacuum oven (89508-426, 600 W from VWR). The dopamine-treated substrate was somewhat rough with some dopamine agglomerates. The static water contact angle on the dopamine-treated substrate was ≈50°, measured on a goniometer (OCA 15) from Dataphysics.

Ink Preparation: The as-received suspensions of PS particles were ultrasonicated for 10 min to redisperse the particles. The suspensions were then diluted by a mixture of ethanol/water with weight fractions ranging from 50 wt%/50 wt% to 100% ethanol to obtain the printable inks with a particle concentration of 10 mg mL^{-1}.

Dual-Droplet Inkjet Printing Process: The inkjet printing platform (Jetlab 4, MicroFab) consists of four printing stations, two of which were used in this study. Supporting droplets and wetting droplets were jetted from two piezoelectric nozzles with different orifice sizes of 30 µm (MJ-ATP-01-80-8MX, MicroFab) and 80 µm (MJ-ATP-01-30-8MX, MicroFab) driven by a waveform generator (Jetdriver III, MicroFab). Firstly, a supporting droplet was generated by jetting multiple bursts of DI water (2000 droplets with a total volume ≈110 nL) on the substrate at a frequency of 500 Hz. Then, wetting droplets containing PS nanoparticles were jetted to the center of the supporting droplet using the 80 µm nozzle at a frequency of 1 Hz. This ensured a complete impact and spreading of the wetting droplet before subsequent droplets. Careful adjustment of the jetting parameters, such as droplet speed and volume, is required for a successful dual-droplet printing in which nearly monolayer ordered depositions are produced. In this work, a jetting speed of ≈1.3 m s^{-1}

and a droplet volume of ≈550 pL (diameter ≈100 µm) were used for the wetting droplet.

In Situ Observation of Droplet Impact and Solvent Evaporation: The wetting and spreading of wetting droplets on the interface of supporting droplets were investigated in situ by a high-speed camera (Phantom, MIRO-LAB3a10) at 5000 fps. The camera was connected to a high-magnification zoom lens (Navitar 6000, 12×) and positioned at an angle of ≈50° from the side of the nozzle to capture the droplet impact dynamics. A regular CMOS camera (THORLABS, DCC1645C) was used to capture the solvent evaporation process at 25 fps.

Morphology Characterization: An ultrahigh-resolution scanning electron microscope (HITACHI SU-70 FE-SEM) with 5 kV and 15 mm scanning distance was used for morphology characterization of the printed patterns. To minimize charging effect of the PS nanoparticles, the samples were coated with platinum using a platinum sputter (Denton Vacuum Desk V) for 60 s.

Optical Spectrum Characterization: A UV–vis spectrophotometer (Evolution 220, Thermo Fisher Scientific) was utilized to analyze the reflection spectrum of the printed films. The light spectrum range was set between 200 and 800 nm with a scanning speed of 400 nm min^{-1}.

Image Analysis: All the image analyses were carried out in Matlab 2015a. The RGB values for each pixel in the optical images were obtained. The BCC intensity was defined as $\sqrt{(B-R)^2+(B-G)^2}$. The intensity profile of the deposit patterns was averaged along the angular direction, i.e., $I(r)=\frac{1}{2\pi}\int_0^{2\pi} i(r,\theta)\,d\theta$, where $i(r,\theta)$ is the local BCC intensity, and r and θ are the cylindrical coordinates on the circular deposition. The intensity profile was then normalized with the maximum intensity $I(r)$ obtained from the printed patterns of Aldehyde/Sulfate-PS nanoparticles since they exhibited the highest color contrast. In addition, the radial distribution of the nanoparticles was normalized with the deposition radius.

COMSOL Simulation: Full-field simulations were conducted for spherical PS particles with diameters of 75 to 325 nm at a 5 nm resolution and wavelengths of 250 to 800 nm at a 10 nm resolution. One perfect unit cell, having one PS particle at the center and one quarter of a PS particle at each of the four corners, was simulated with periodic conditions to make a perfect hexagonal closely packed surface. A port was used to excite the surface perpendicularly from the top, and a perfect layer was used beyond the substrate to limit reflection to that of the surface. The reflection intensity was calculated based on the perpendicular scattering from the port to itself.

Supporting Information

Supporting Information is available from the Wiley Online Library or from the authors.

Acknowledgments

The authors are grateful for the support of the National Science Foundation under Grant No. CMMI-1634938. N.K. acknowledges support from the Virginia Microelectronics Consortium Seed Grant. The authors also thank Drs. Christina Tang and Qijin Huang for insightful discussions. T.N.N. and H.Z. had done the initial planning of dual-droplet printing of functional materials. H.Z. supervised the project and wrote the manuscript. K.N.A.-M. designed and conducted the experiments, and wrote the manuscript. R.R.S. and N.K. conducted the COMSOL simulation and contributed to the manuscript writing. All the authors discussed, commented, and agreed upon the content in this manuscript.

Conflict of Interest

The authors declare no conflict of interest.

Keywords

air–droplet interfaces, dual-droplet printing, self-assembly, supporting droplets, wetting droplets

Received: November 27, 2017
Revised: January 19, 2018

---

[1] R. D. Deegan, O. Bakajin, T. F. Dupont, G. Huber, S. R. Nagel, T. A. Witten, *Nature* **1997**, *389*, 827.
[2] R. D. Deegan, *Phys. Rev. E* **2000**, *61*, 475.
[3] B. J. Fischer, *Langmuir* **2002**, *18*, 60.
[4] R. G. Larson, *AIChE J.* **2014**, *60*, 1538.
[5] S. Lin, K. Yang, L. Chen, *J. Phys. Chem. C* **2015**, *119*, 3050.
[6] N. D. Patil, P. G. Bange, R. Bhardwaj, A. Sharma, *Langmuir* **2016**, *32*, 11958.
[7] E. L. Talbot, H. N. Yow, L. Yang, A. Berson, S. R. Biggs, C. D. Bain, *ACS Appl. Mater. Interfaces* **2015**, *7*, 3782.
[8] M. Liu, J. Wang, M. He, L. Wang, F. Li, L. Jiang, Y. Song, *ACS Appl. Mater. Interfaces* **2014**, *6*, 13344.
[9] P. He, B. Derby, *Adv. Mater. Interfaces* **2017**, *4*, 1700944.
[10] M. Kuang, J. Wang, B. Bao, F. Li, L. Wang, L. Jiang, *Adv. Opt. Mater.* **2014**, *2*, 34.
[11] Y. Li, Y.-J. Sheng, H.-K. Tsao, *Langmuir* **2013**, *29*, 7802.
[12] J. Park, J. Moon, *Langmuir* **2006**, *22*, 3506.
[13] T. Still, P. J. Yunker, A. G. Yodh, *Langmuir* **2012**, *28*, 4984.
[14] M. Majumder, C. S. Rendall, J. A. Eukel, J. Y.L. Wang, N. Behabtu, C. L. Pint, T. Liu, A. W. Orbaek, F. Mirri, J. Nam, A. R. Barron, R. H. Hauge, H. K. Schmidt, M. Pasquali, *J. Phys. Chem. B* **2012**, *116*, 6536.
[15] R. Bhardwaj, X. Fang, P. Somasundaran, D. Attinger, *Langmuir* **2010**, *26*, 7833.
[16] H. Kim, F. Boulogne, E. Um, I. Jacobi, E. Button, H. A. Stone, *Phys. Rev. Lett.* **2016**, *116*, 124501.
[17] T. P. Bigioni, X. Lin, T. T. Nguyen, E. I. Corwin, T. A. Witten, H. M. Jaeger, *Nat. Mater.* **2006**, *5*, 265.
[18] J. W. Boley, S. H. Hyun, E. L. White, D. H. Thompson, R. K. Kramer, *Appl. Mater. Interfaces* **2016**, *8*, 34171.
[19] Y. Li, Q. Yang, M. Li, Y. Song, *Sci. Rep.* **2016**, *6*, 24628.
[20] M. Anyfantakis, Z. Geng, M. Morel, S. Rudiuk, D. Baigl, *Langmuir* **2015**, *31*, 4113.
[21] M. Anyfantakis, L. Marichal, L. Kiger, M. Morel, S. Rudiuk, D. Baigl, *J. Am. Chem. Soc.* **2016**, *138*, 11623.
[22] H. Minemawari, T. Yamada, H. Matsui, J. Tsutsumi, S. Haas, R. Chiba, R. Kumai, T. Hasegawa, *Nature* **2011**, *475*, 364.
[23] Y. Noda, H. Minemawari, H. Matsui, T. Yamada, S. Arai, *Adv. Funct. Mater.* **2015**, *25*, 4022.
[24] G. Vazquez, E. Alvarez, J. M. Navaza, *J. Chem. Eng. Data* **1995**, *40*, 611.
[25] Y. Lin;, H. Skaff;, T. Emrick;, A. D. Dinsmore, T. P. Russell, *Science* **2003**, *299*, 226.
[26] X. Fang, B. Li, J. Wu, C. Maldarelli, J. C. Sokolov, M. H. Rafailovich, P. Somasundaran, *J. Phys. Chem. Lett. B* **2009**, *113*, 9636.
[27] J. C. Loudet, A. G. Yodh, B. Pouligny, *Phys. Rev. Lett.* **2006**, *97*, 18304.
[28] L. Su, Y. Yu, Y. Zhao, F. Liang, X. Zhang, *Sci. Rep.* **2016**, *6*, 24420.
[29] D. Liu, C. Li, F. Zhou, T. Zhang, G. Liu, W. Cai, Y. Li, *Adv. Mater. Interfaces* **2017**, *4*, 1600976.
[30] Y. Kim, H. Jung, C. W. Ahn, H. Jeon, *Adv. Mater. Interfaces* **2017**, *4*, 1700342.
[31] J. Hou, M. Li, Y. Song, *Angew. Chem., Int. Ed.* **2017**, *57*, 2544.

[32] L. Wang, J. Wang, Y. Huang, M. Liu, M. Kuang, Y. Li, L. Jiang, Y. Song, *J. Mater. Chem.* **2012**, *22*, 21405.
[33] L. Bai, Z. Xie, W. Wang, C. Yuan, Y. Zhao, Z. Mu, Q. Zhong, Z. Gu, *ACS Nano* **2014**, *8*, 11094.
[34] C. Arsenault, D. P. Puzzo, I. A. N. Manners, G. A. Ozin, *Nat. Photonics* **2007**, *1*, 468.
[35] S. Y. Lee, S. Kim, H. Hwang, J. Y. Sim, S. Yang, *Adv. Mater.* **2014**, *26*, 2391.
[36] S.-J. Kim, B.-H. Kim, S.-W. Kim, S.-J. Shin, R. Street, A. Salleo, S. Ready, *J. Imaging Sci. Technol.* **2010**, *54*, 50307.
[37] H. Nam, K. Song, D. Ha, T. Kim, *Sci. Rep.* **2016**, *6*, 30885.
[38] Y. Masuda, T. Itoh, K. Koumoto, *Langmuir* **2005**, *21*, 4478.
[39] I. B. Burgess, L. Mishchenko, B. D. Hatton, M. Kolle, M. Lon, J. Aizenberg, *J. Am. Chem. Soc.* **2011**, *133*, 12430.
[40] M. Kuang, Y. Song, in *Nanomaterials for 2D and 3D Printing*, (Eds: S. Magdassi, A. Kamyshny), Wiley-VCH Verlag GmbH & Co. KGaA, Weinheim, Germany **2017**, Ch. 9.
[41] C. Matzler, MATLAB functions for Mie scattering and absorption **2002**. http://arrc.ou.edu/~rockee/NRA_2007_website/Mie-scattering-Matlab.pdf (accessed: November 2017).
[42] H. N. Umh, S. Yu, Y. H. Kim, S. Y. Lee, J. Yi, *Appl. Mater. Interfaces* **2016**, *8*, 15802.